



# Analysis of near-field strong motion observations and damages of Menyuan earthquake on 8 January 2022 based on dense MEMS stations

Dongwang Tao · Jianqi Lu · Qiang Ma · Jilong Li · Wen Peng · Shanyou Li

Received: 22 March 2022 / Accepted: 15 September 2022 / Published online: 1 October 2022  
© The Author(s), under exclusive licence to Springer Nature B.V. 2022

**Abstract** The 2022  $M_S$  6.9 ( $M_W$  6.6) Menyuan earthquake occurred in the northeastern Tibetan Plateau and was recorded by a large number of recently installed micro-electro-mechanical system (MEMS) stations within 100-km fault distance. By comparing the pre-event noises and earthquake signals in time domain and frequency domain, it is found that the records are feasible to be used to analyze ground motion parameters. These records

provide a database for analyzing the main features of the ground motions recorded by MEMS stations, in terms of ground motion models (GMMs), near-field impulsive characteristics, and seismic intensities. The observed ground motion parameters are compared with the predicted values by Boore et al. (Earthq Spectra 30(3):1057–1085, 2014) GMM model, and it is found that the GMM model predicts higher shaking at the short and medium periods and lower shaking at the long periods. However, the shaking intensities at the short periods for Central Italy 2016 earthquake sequence are well predicted by the GMM model. The observed Chinese seismic intensity (CSI) by instruments is compared with modified Mercalli intensity (MMI) and surveyed macroseismic intensity (SMI), and it is found that CSI values are 0.73 intensity unit greater than MMI values and high SMI can be well predicted by CSI. Ground motions at three stations

## Highlights

- Records from MEMS stations are feasible for analyzing ground motion parameters.
- The PGAs and PSAs at short and medium periods are noticeably overestimated by GMM.
- Pulse-like ground motions are identified, and the station closest to the epicenter has pulse indicator greater than 0.85 at almost all orientations.

**Supplementary Information** The online version contains supplementary material available at <https://doi.org/10.1007/s10950-022-10113-9>.

D. Tao · J. Lu · Q. Ma (✉) · J. Li · W. Peng · S. Li  
Key Laboratory of Earthquake Engineering and Engineering Vibration, Institute of Engineering Mechanics, China Earthquake Administration, Harbin 150080, China  
e-mail: maqiang@iem.ac.cn

D. Tao  
e-mail: taodongwang@iem.ac.cn

J. Lu  
e-mail: ljqsjy@163.com

J. Li  
e-mail: 1051334119@qq.com

W. Peng  
e-mail: w\_peng0705@163.com

S. Li  
e-mail: lishanyou@126.com

D. Tao · J. Lu · Q. Ma · J. Li · W. Peng · S. Li  
Key Laboratory of Earthquake Disaster Mitigation, Ministry of Emergency Management, Harbin 150080, China

are classified as pulse-like based on the methodology by Baltzopoulos et al. (Bull Seismol Soc Am 110(4):1495–1505, 2020), and whether the pulses have been caused by forward directivity or fling step is discussed, and only one station may be directivity related and the other two are still inconclusive. Finally the earthquake damage of a high-speed railway bridge in the intensity IX area is presented.

**Keywords** Menyuan earthquake · MEMS · Near-field · Pulse-like · GMM · Seismic intensity

## 1 Introduction

According to China Earthquake Networks Center (CENC), on 8 January 2022 at 01:45 a.m. Beijing time, a strong earthquake with surface wave magnitude  $M_S$  6.9 occurred at Menyuan County in the northeast of Qinghai province in China. The earthquake hypocenter was located at  $37.77^\circ$  N and  $101.26^\circ$  E with a depth of 10 km, about 140 km northwest of Xining City, the provincial capital of Qinghai. The maximum surveyed macroseismic intensity (SMI) was IX of Chinese intensity scale, equivalent to modified Mercalli intensity (MMI) IX (GB/T 17742–2020 2020). The earthquake occurred in Qilian Mountain seismic belt along the margin of northeastern Tibetan Plateau and was well recorded by a dense low-cost micro-electro-mechanical system (MEMS) strong motion stations, which have been constructed as part of the National System for Rapid Seismic Intensity Report and Earthquake Early Warning project led by China Earthquake Administration. There were 79 MEMS stations with epicentral distances less than 100 km and the average interstation distance was 14.3 km. The nearest MEMS station was QHC0028 with epicentral distance of 7.8 km, and 5 stations were within 20 km, and 18 stations within 50 km. On the other hand, the former National Strong-Motion Observation Network System (NSMONS) of China, aiming to monitor earthquakes and collect strong motion recordings with traditional force-balanced accelerometers (FBA), had an average station spacing of 50 km to hundreds of kilometers (Wen and Ren 2014), and it was difficult to record near-field strong motions in some area like Qinghai province. For example, the nearest stations were with epicentral distances

of 176 km and 350 km for 14 April 2010  $M_S$  7.1 Qinghai Yushu earthquake and 2 May 2021  $M_S$  7.4 Qinghai Maduo earthquake, respectively. This  $M_S$  6.9 Menyuan earthquake is the first time that MEMS stations record so many near-field strong motions for earthquake larger than  $M_S$  6.5, and these recordings provide an excellent database for analyzing near-field strong motion characteristics at northeastern Tibetan Plateau where strong ground motion records were rare before.

MEMS accelerometers have been implemented in a variety of industrial and scientific fields due to low-cost and high-precision capability. Holland (2003) introduced MEMS accelerometers to recording earthquake data in 2001 and found that the Applied MEMS, Inc., model SF1500A accelerometers were suited for earthquake ground motion recording. Since then, MEMS accelerometers have been increasingly used for seismic applications. Significant examples of MEMS networks include Quake-Catcher Network (QCN) (Cochran et al. 2009), Self-Organizing Seismic Early Warning Information Network (SOSEWIN) (Fleming et al. 2009), P-alert network (Wu et al. 2013), Community Seismic Network (CSN) (Clayton et al. 2015), and MEMS Accelerometer Mini-Array (MAMA) (Nof et al. 2019). It has been generally acknowledged that low-cost MEMS sensors with resolutions of 16 are able to detect moderate to large earthquake at distances of dozens of kilometers away (Evans et al. 2014; Yildirim et al. 2015; Nof et al. 2019). By comparing the ground motions recorded by QCN MEMS accelerometers with traditional GeoNet accelerometers from  $M$  7.1 Darfield earthquake, Cochran et al. (2011) found that observed peak ground acceleration (PGA) and peak ground velocity (PGV) amplitudes and root mean square (RMS) scatter were comparable between the two type of instruments, and closely spaced stations gave similar waveforms and pseudo-spectral accelerations (PSAs). Wu et al. (2016) compared ground motions recorded by P-alert network MEMS accelerometers with conventional FBA instruments from  $M$  6.4 Meinong earthquake, and found that the performance of P-alert network proved efficiency in terms of earthquake early warning, near real-time shake maps, and strong motion data for research purposes. Nof et al. (2019) conducted field test of MAMA network and found that the mean power spectral density (PSD) levels for

MEMS accelerometers were  $-73$  to  $-80$  dB and the MAMA network had the capability to obtain useful earthquake signals of small magnitude events. By comparing the mean PSD of MEMS accelerometers with those of conventional Epi-sensors, Nof et al. (2019) found that recorded waveforms of MAMA network were reliable at stations with 100-km epicentral distance in an  $M$  6.5 earthquake. Pierleoni et al. (2018) compared the low-cost MEMS accelerometers with co-sited high-performance FBA during seismic events of 2016–2017 in central Italy, and found that MEMS accelerometers demonstrated performance very close to traditional instruments in terms of waveform correlation, strong motion parameter estimation, and spectral analysis. The analysis of thousands of seismic event indicated that the MEMS accelerometers were able to record events of local magnitude greater than  $M$  2.5 at relatively short distance less than 40 km. For an  $M$  5.9 earthquake, the acceleration waveforms recorded by MEMS at one station with epicentral distance of 21.6 km were almost the same as FBA instrument at the same station. Peng et al. (2019) evaluated the performance of a dense MEMS-based seismic array deployed in the Sichuan-Yunnan region of China, and found that the records by MEMS were consistent with the data obtained by collocated traditional FBA even for stations with an epicentral distance of more than 150 km. Peng et al. (2020) also tested and verified the reliability and effectiveness of a hybrid system with MEMS sensors and broadband seismographs in the Sichuan-Yunnan region for earthquake early warning application. Since CSN recorded high-quality strong motions during the 2019 Ridgecrest earthquake sequence, Filippitzi et al. (2021) studied ground motion characteristics in urban Los Angeles using dense CSN records together with high-quality Southern California Seismic Network and California Strong Motion Instrumentation Program records. Using the above three ground motion database, Kohler et al. (2020) revealed that the shaking of high-rise buildings was amplified in Los Angeles area due to long-period amplification. The two CSN-related articles analyzed PSAs and site amplification factors of ground motion up to period of 8 s, implying that the low-frequency contents around 0.1 Hz measured by MEMS sensors were reliable. The above studies have demonstrated that the low-cost MEMS accelerometers are able to be efficient

for recording strong ground motion shaking. For an  $M_S$  6.9 earthquake, the records by MEMS sensors within epicentral distance of 100 km are able to analyze strong ground motion parameters such as PGAs, PGVs, PSAs, and seismic intensities.

The epicenter of  $M_S$  6.9 Menyuan earthquake was  $\sim 340$  km west of the 26 December 1920  $M$  8.5 Gansu Haiyuan earthquake and  $\sim 83$  km west of the 23 May 1927  $M$  8.0 Gansu Gulang earthquake both in the Qilian-Haiyuan fault zone. The nearby faults close to the epicenter were left-lateral strike-slip fault Lenglongling Fault (LLLF) and its affiliated fault Northern Lenglongling Fault (NLLLF), left-lateral strike-slip fault Tuolaishan Fault (TLSF), and thrust fault Northern Qilian-shan Fault (NQLSF) (Zhang et al. 2020). NLLLF caused two thrust earthquakes in Menyuan County. One was 26 August 1986  $M_S$  6.4 earthquake 23 km away from this event, and the other was 21 January 2016  $M_S$  6.4 earthquake 33 km away. However, these two earthquakes did not rupture to the surface (Zhang et al. 2020). Surface ruptures of the 8 January 2022 Menyuan  $M_S$  6.9 earthquake along the northwest-west–southeast-east direction were about 22 km provided by the remote sensing image by National Institute of Natural Hazards (see Data and resources), suggesting that the causative seismogenic faults might be the left-lateral strike-slip LLLF and TLSF. Focal mechanism solution from US Geological Survey (USGS) reported that moment magnitude  $M_W$  was 6.6 and the nodal planes (strike/dip/rake) were  $104^\circ/88^\circ/15^\circ$  and  $13^\circ/75^\circ/178^\circ$  (see Data and resources). The long axis of the isoseismic line with SMI VI was about 200 km, and the short axis was about 153 km (see Data and resources). As the event occurred in a sparsely populated area, the casualties caused by the earthquake were relatively light. However, key infrastructures such as high-speed railway and highway transportation systems near the epicenter zone were severely damaged. The deck beams of Liuhuanggou high-speed railway bridge near Lenglongling Mountain were seriously displaced and tilted due to the failures of bridge bearings, and the railway tracks were severely twisted and partially broken (see Data and resources).

In this study, first, the pre-event noise levels and earthquake signals are compared in time domain and frequency domain to check the quality of MEMS

strong motions. Then, the observed ground motion parameters such as PGA, PGV, 5% damped PSAs, and significant duration (SD) are compared with the predicted values by ground motion models (GMMs), and the GMMs' performance in the Menyuan earthquake is also compared with 2016 Central Italy sequence which have hundreds of near-field strong motion records. Later, the Chinese seismic intensity (CSI) based on the ground motion to intensity conversion equation (GMICE) are compared with MMI of Worden et al. (2012) and SMI. Potential pulse-like ground motions are then identified based on the methodology by Baltzopoulos et al. (2020), and the forward directivity and fling step effect on the pulses are discussed. Finally, the earthquake damage of a high-speed railway bridge in the intensity IX area is presented.

## 2 Observed strong motion recordings

The deployed MEMS accelerometer integrates three orthogonal MEMS acceleration sensors and a built-in 24-bit data analog-to-digital converter. Full-scale acceleration range is  $\pm 2$  g for horizontal components and  $-3$  g–g for vertical component. The frequency band is from DC to 40 Hz. The traditional strong motion station is equipped with three-component SLJ-100 FBA and a 18-bit resolution ETNA recorder, and the full scale is  $\pm 2$  g and the dynamic range is 108 dB (Wen et al. 2010). In the instrument performance test of MEMS accelerometers conducted at Institute of Engineering Mechanics, China Earthquake Administration, the average self-noise level was  $2.8 \times 10^{-2}$  cm/s<sup>2</sup>, lower than the Phidgets noise level of  $1.0 \times 10^{-1}$  cm/s<sup>2</sup> from CSN (Clayton et al. 2015), and the dynamic range was about 97 dB. The self-noise level was close to the lower limit of instrument self-noise of MEMS station in central Italy, about  $2.0 \times 10^{-2}$  cm/s<sup>2</sup>, presented in Pierleoni et al. (2018). In the shaking table tests, which used input sine wave motions with various amplitudes and frequencies and compared the amplitude responses of MEMS accelerometers with input reference, the amplitude ratios were  $-0.1$  to  $0.1$  dB for frequency band 1.0–10.0 Hz and  $-1.5$  to  $1.5$  dB for 10.0–40.0 Hz. Due to the limitation of shaking table condition, amplitude-frequency characteristics of the MEMS accelerometers below 1.0 Hz were not

conducted. In the tested frequency range, the MEMS accelerometers had basically the similar amplitude-frequency behavior to Phidgets as shown in Evans et al. (2014). The real-time data recorded by the MEMS stations are transferred through 3G/4G Internet signals to Earthquake Data Processing Center. The sampling frequency is 100 Hz, and the output sensitivity is 500 counts/(cm/s<sup>2</sup>). During the  $M_s$  6.9 Menyuan earthquake, there are 79 MEMS stations within the Joyner-Boore fault distance ( $R_{JB}$ ) of up to 100 km. The values of  $R_{JB}$  are calculated based on the ruptured fault plane given by Zhang et al. (2022). Two stations with exceptional low amplitude comparing with nearby stations and signal to noise ratio (SNR) less than 3 are discarded. Here, SNR is defined as the ratio of root mean square (RMS) of 20-s earthquake signal after P-wave onset over RMS of 20-s pre-event noise. The locations of the selected 77 stations are plotted in Fig. 1, and the station codes, longitude, latitude, and  $R_{JB}$  are shown in Table S1 (available in the electronic supplement to this article). The recordings at these 77 stations are used to analyze near-field strong motion characteristics and shaking intensities. All acceleration records are processed using a second-order Butterworth filter with a bandwidth of 0.1–40.0 Hz to calculate ground motion parameters such as PGAs, PGVs, PSAs, and SDs. The velocities are obtained by single integration of the filtered accelerations. The largest PGA is 475.1 cm/s<sup>2</sup> of the NS component at QHC0028 site, whereas the largest PGV is 27.9 cm/s of the NS component at QHC0036 station. Since the S-wave velocity measurements for the recently installed MEMS stations are not available, the recommended  $V_{S30}$ , the time-averaged shear wave velocity in the upper 30 m, obtained using proxies based on topographic slope (Wald and Allen 2007) are used to represent site conditions. The  $V_{S30}$  and National Earthquake Hazards Reduction Program (NEHRP) categories are listed in Table S1. Most MEMS stations belong to category C with 62 stations, 11 stations as category D, and 4 stations as category B. The average  $V_{S30}$  for the all 77 stations is 490 m/s.

The north–south (NS), east–west (EW), and up–down (UD) component acceleration of pre-event noises and earthquake signals at four stations are plotted in Fig. 2. The  $R_{JB}$  for stations QHC0028, QHC0029, QHC0036, and QHC0002 are 5.0, 13.4,

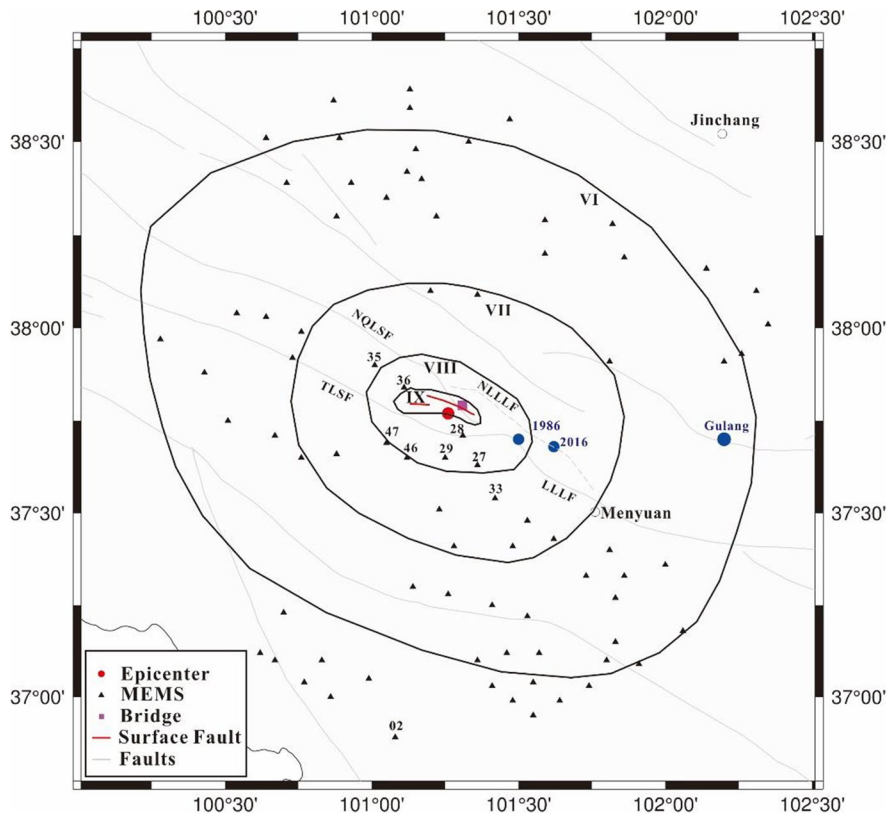


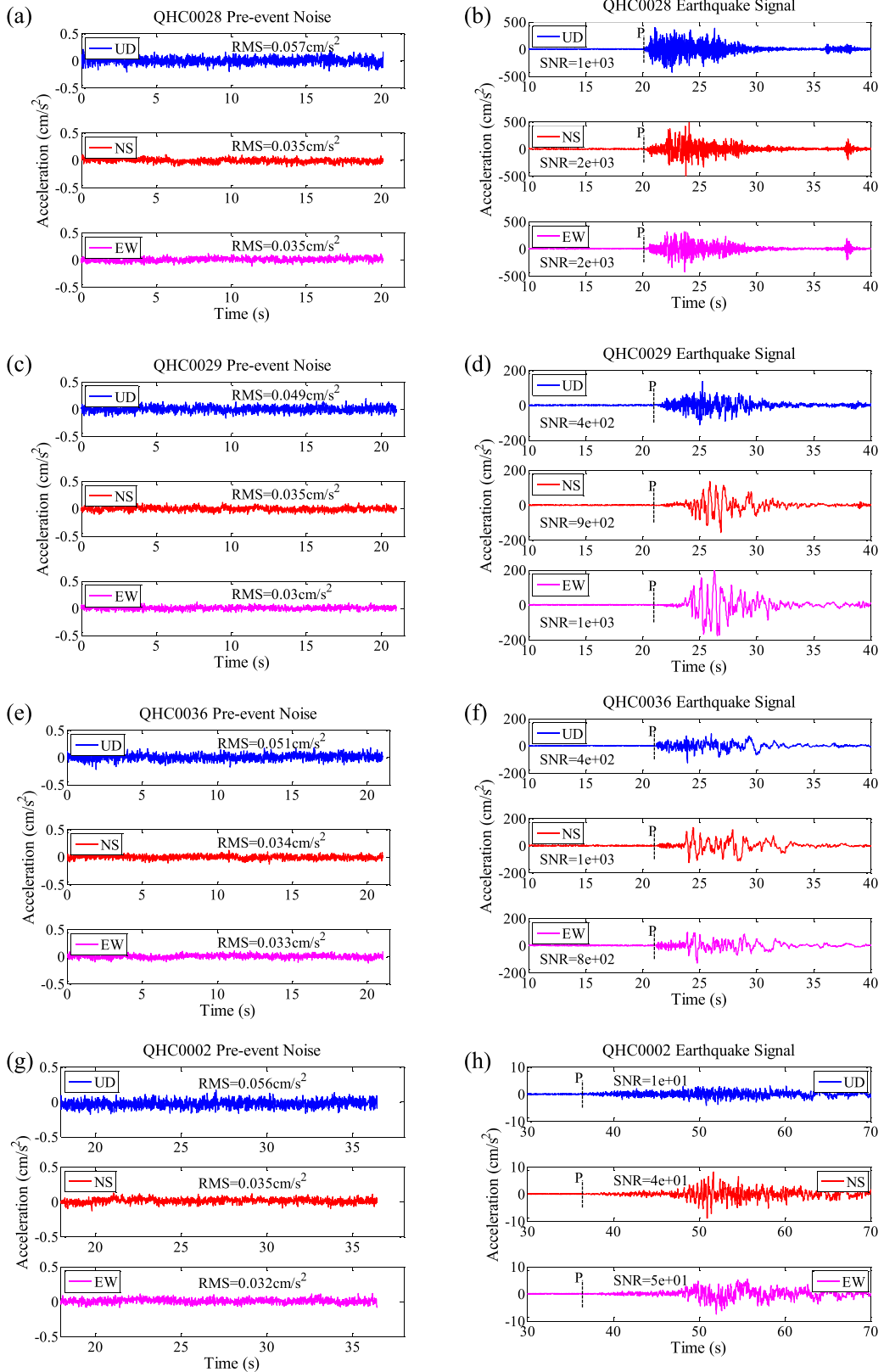
**Fig. 1** Distribution of MEMS stations and surveyed macroseismic intensity (SMI). The red circle shows the epicenter of the  $M_S$  6.9 Menyuan earthquake, and the red line for the surface ruptures. The triangulars show the location of MEMS stations, and the numbers 02, 27, 28, 29, 33, 35, 36, 46, and 47 for QHC0002, QHC0027, QHC0028, QHC0029, QHC0033, QHC0035, QHC0036, QHC0046, and QHC0047 stations. The magenta square shows the high-speed railway bridge with

severe damage. The blue circles show historical earthquakes, and 1986, 2016, and Gulang for 26 August 1986  $M_S$  6.4 Menyuan earthquake, 21 January 2016  $M_S$  6.4 Menyuan earthquake, and 23 May 1927  $M$  8.0 Gulang earthquake. The gray lines show active faults from Deng et al. (2003). Abbreviations of the fault names are LLLF for Lenglongling fault, NLLLF for Northern Lenglongling fault, TLSF for Tuolaishan fault, and NQLSF for Northern Qilianshan fault (see Data and resources)

4.7, and 98.9 km, respectively. Station QHC0002 is the station with largest  $R_{JB}$  distance of the all 77 stations. Though with different  $R_{JB}$  distances, the RMS of pre-event noise for horizontal components at these four station are at the same level, about  $0.035 \text{ cm/s}^2$ . This noise level is of the same order of magnitude as that of deployed GL-P2B which can be classified as a type of Class-B sensor presented in Peng et al. (2019). SNR at three stations for  $R_{JB} \sim 10 \text{ km}$  (i.e., QHC0028, QHC0029, and QHC0036) are larger than 400 for all three components. SNR of two horizontal components at QHC0002 station are larger than 40, and the PGAs are larger than  $7 \text{ cm/s}^2$ . In the performance of evaluation of MEMS stations, Pierleoni et al. (2018)

selected ground motions with  $\text{SNR} > 3$  and amplitude larger than  $0.065 \text{ cm/s}^2$ . For all the 77 MEMS stations in the Menyuan earthquake, the SNR are larger than 3 and amplitudes are much larger than  $0.065 \text{ cm/s}^2$ . In this regard, the ground motions recorded by MEMS stations are feasible to be used to analyze ground motion parameters.

Fourier spectra of pre-event noises and earthquake signals in the EW components at the four stations are shown in Fig. 3. In the frequency band of 0.1–30 Hz, the amplitude of earthquake signal is much larger than that of pre-event noise at QHC0028, QHC0029, and QHC0036 stations. At QHC0002 station, the Fourier spectra of earthquake signal in the frequency band larger than 20 Hz are contaminated by pre-event





◀**Fig. 2** Pre-event noises and earthquake signals at four near-field stations (a–b) QHC0028, (c–d) QHC0029, (e–f) QHC0036, and (g–h) QHC0002. The dashed vertical line shows the arrival time of P-wave

noise. In this regard, ground motions in frequency band within 0.1–20 Hz are credible for calculating ground motion parameters. It is noted that QCN MEMS accelerometers are also able to detect acceleration in frequency band within 0.1–20 Hz (Cochran et al. 2009). The energies of earthquake signals in the frequency band 0.2–4 Hz for the three nearest stations are basically comparable; however, QHC0028 station has much higher frequencies > 4 Hz than the other two stations.

To show the time-varying frequency in the ground motions recorded by the MEMS accelerometers, the time–frequency energy distributions for the EW components at the four stations based on complex continuous wavelet transform are shown in Fig. 4. WaveLab package is used to implement wavelet transform, and the Gabor wavelet is chosen as the mother wavelet, and the parameter determining the width of frequency band is chosen as 1 to obtain both good time and frequency resolution (Buckheit and Donoho 1995; Li et al. 2013; see Data and resources). The energies for the QHC0028 station are mainly concentrated in the time–frequency windows with frequency band 10–20 Hz and time interval 22–28 s, while much narrower and lower frequency band 1–2 Hz and time interval 24–28 s for QHC0029 station. Since the subtotal energies in the frequency band of 0.1–1 Hz are significantly smaller than other higher frequency bands at these two stations, the energies below frequency of 1 Hz cannot be seen in the colored contour plot. At QHC0036 station, the energies are mainly in higher frequency band 15–20 Hz for the first few seconds, then in lower frequency band 1–5 Hz during 22–30 s. It is noted that the time–frequency energy distributions at QHC0028 and QHC0036 stations show quite different characteristics though the two stations have almost the same fault distance, and this implies that the high frequency energy is attenuated rapidly even in the near-field zone with  $R_{JB} \sim 10$  km. At QHC0002 station, the energies are mainly concentrated in the time–frequency windows with frequency band 1–8 Hz and time interval 49–56 s, and the low-frequency energy in frequency band 0.1–0.5 Hz exists during 55–70 s, and the characteristics of energy

release are consistent with the general understanding that high-frequency contents are dominant in the early stage and lower frequency contents become more dominant in the later stage (Zhou and Adeli 2003). The four contour plots also imply that the soil condition at QHC0002 ( $V_{S30} = 615$  m/s) is the stiffest, followed by stations QHC0036 ( $V_{S30} = 487$  m/s) and QHC0029 ( $V_{S30} = 366$  m/s), which is consistent with the  $V_{S30}$  values. The energies of the ground motions at station QHC0028 are dominated by source effect, and it is difficult to compare soil condition from contour plots.

### 3 Comparison of ground motion parameters with GMMs

To compare the observed ground motion parameters with established GMMs, Next Generation Attenuation-West 2 (NGA-West2) model by Boore et al. (2014) (hereinafter BSSA14) and Afshari and Stewart (2016) (hereinafter AS16) are used to predict PGA, PGV, PSAs, and SD values. The RotD50 ground motion parameters proposed by Boore (2010), which is the 50th percentile of the median value of horizontal ground motions over all rotations, are calculated for PGAs, PGVs, PSAs, and 5–95% SDs (Trifunac and Brady 1975) for GMM comparisons.

The residuals for the observed PGAs, PGVs, and PSAs at periods of 0.3, 1.0, and 3.0 s and SDs with predictions estimated by the BSSA14 and AS16 models are shown in Fig. 5. The options are set as (1)  $M_W = 6.6$ ; (2) strike-slip fault type; (3) regional adjustment of anelastic attenuation for China; and (4)  $Z_{1.0}$  is not considered (taken as  $-1$ ) in Boore's Fortran package for BSSA14 loop calculation (Boore et al. 2014); see Data and resources). The PGAs and PSAs at short and medium periods 0.3 s and 1.0 s are noticeably overestimated by the BSSA14 model; however, PSAs at long-period 3.0 s are consistent with the prediction model. The observed PGVs are slightly less than the predicted values. The SDs are generally well predicted by the AS16 model. Ren et al. (2018) reported similar characteristics for the Jiuzhaigou earthquake. The Jiuzhaigou earthquake occurred on 8 August 2017 in the same Qinghai-Tibet earthquake region, and the magnitude was  $M_W$  6.5 and it was also a left-lateral strike-slip earthquake. However, the average PGA and PGV values for July

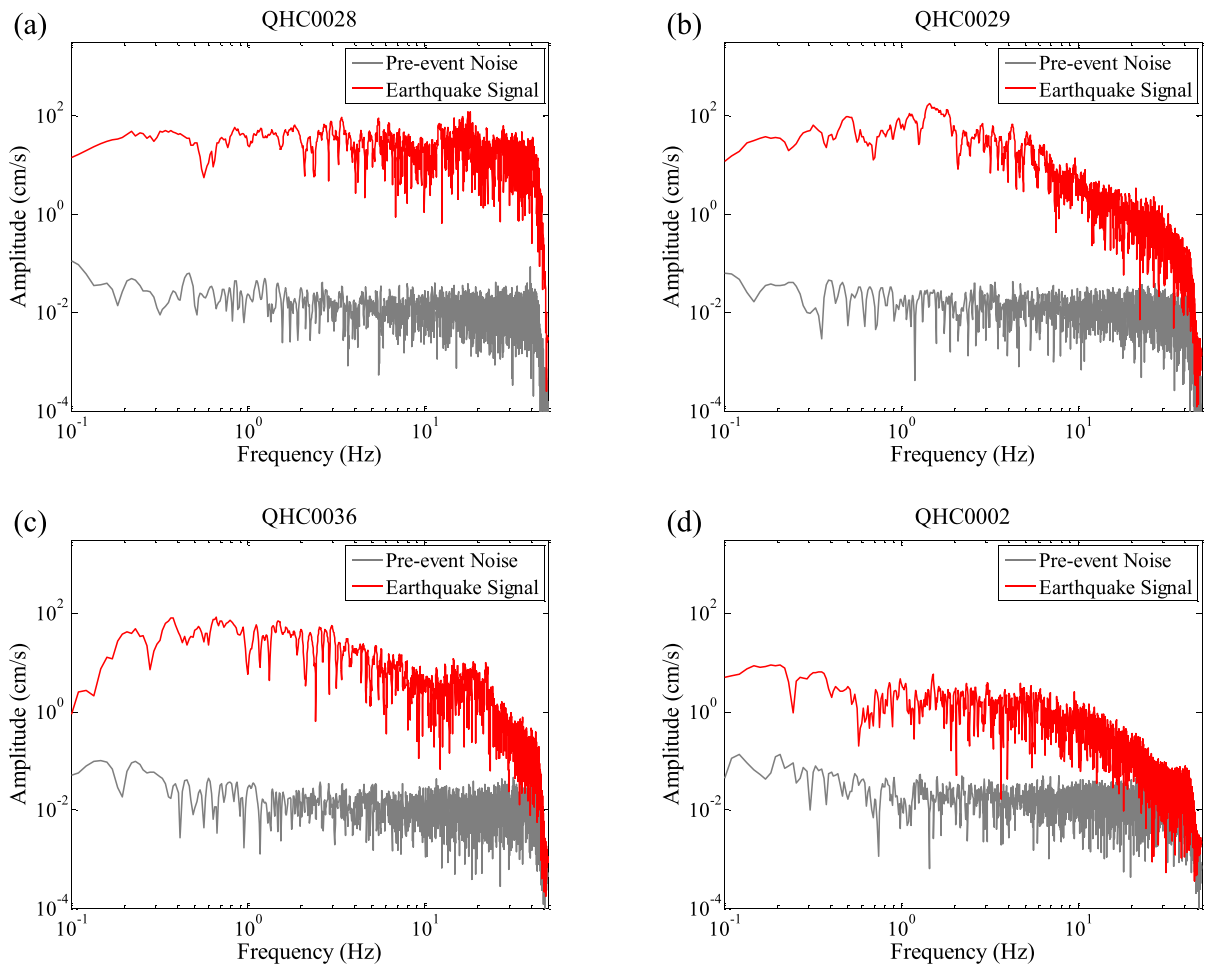


**Fig. 3** Fourier spectra of pre-event noises and earthquake signals in the EW components at (a) QHC0028, (b) QHC0029, (c) QHC0036, and (d) QHC0002 stations

2019 Ridgecrest earthquake sequence were generally consistent with the BSSA14 model (Hough et al. 2020a, b).

The total residuals expressed as natural logarithm of observed values over the median value predicted by the BSSA14 models are calculated for the PGAs and PSAs at periods up to 5 s. To compare GMMs for recent China earthquake with same magnitude and mechanism and earthquakes in other region, the total residuals of ground motions at stations with  $R_{JB} < 100$  km are calculated for the Jiuzhaigou earthquake and Central Italy 2016 earthquake sequence (Luzi et al. 2017; Ren et al. 2018). In the Italy sequence, three main events 24 August  $M_W$  6.0, 26 October  $M_W$  5.9, and 30 October  $M_W$  6.5 earthquakes

are considered since there are hundreds of near-field strong motions within  $R_{JB} < 100$  km for each earthquake, and the observed ground motion parameters are obtained from Engineering Strong-Motion (ESM) database flatfile (Luzi et al. 2017; see Data and resources).

The total residuals are then separated into between-event residuals  $\delta B$  and within-event residuals  $\delta W$ , according to the definition by Al Atik et al. (2010). The  $\delta B$  terms indicate the knowledge that events with similar source characteristics may have overall higher or lower ground motion parameters compared with GMMs, while  $\delta W$  terms represent the spatial variability of these parameters at different locations within the same event (Engler et al. 2022).



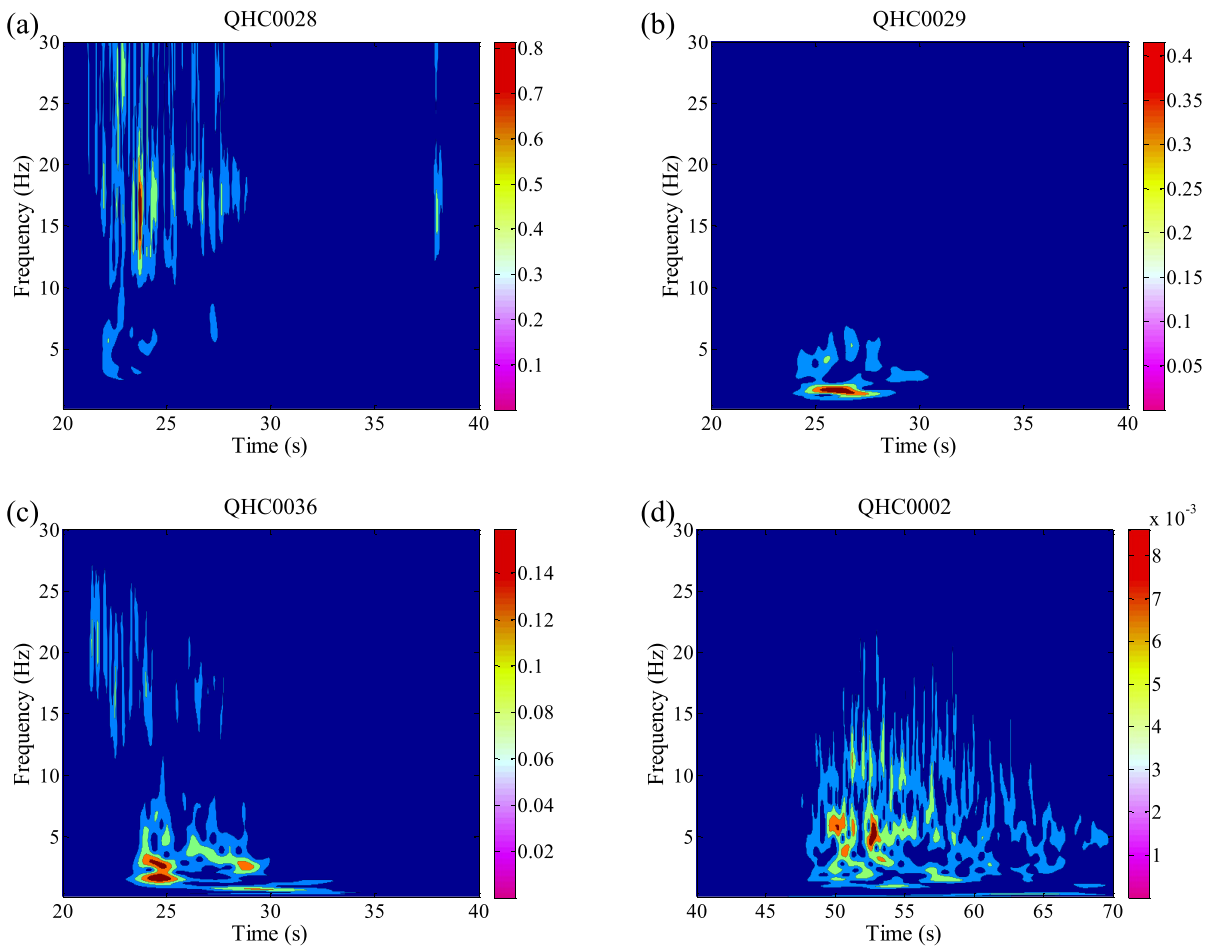


**Fig. 4** Time–frequency energy distributions for the EW components at (a) QHC0028, (b) QHC0029, (c) QHC0036, and (d) QHC0002 stations

The  $\delta B$  values for the Menyuan, Jiuzhaigou earthquakes, and Central Italy 2016 earthquake sequence are shown in Fig. 6. The  $\delta B$  values are almost negative except PSAs at periods larger than 3.0 s for the Menyuan earthquake, while  $\delta B$  values are all negative, with greater deviation, for the Jiuzhaigou earthquake. Generally, the BSSA14 model predicts higher shaking at period less than 3 s for the two earthquake; however, the shaking at long period larger than 3 s for the Menyuan earthquake is slightly underestimated. Two other NGA-West2 models by Abrahamson et al. (2014) and Chiou and Youngs (2014) also give negative between-event residuals for the two Chinese mainland events as shown in Appendix Fig. 13. Ren et al. (2018) reported that Abrahamson et al. (2014) model also predicted higher shaking for the Jiuzhaigou earthquake. This systematic bias may be caused

by the lack of mainland China ground motion records in the NGA-West2 models. Compared with the Jiuzhaigou earthquake, the ground motion parameters for the Menyuan earthquake are predicted much better by the BSSA14 model. For Central Italy 2016 earthquake sequence, the PGAs and PSAs at periods less than 1.0 s are well predicted by the BSSA14 model, and the PSAs at periods larger than 1.0 s are slightly underestimated.

The within-event residuals as a function of  $R_{JB}$  distance for PGAs, PGVs, and PSAs at periods of 0.3, 1.0, and 3.0 s and SD for the Menyuan earthquake and Central Italy 2016 earthquake sequence are plotted in Fig. 7. In general, the binned mean residuals are close to zero for the six ground motion parameters. For the PGAs and PSAs at short periods, the within-event residuals have positive trends at short distances while negative trends

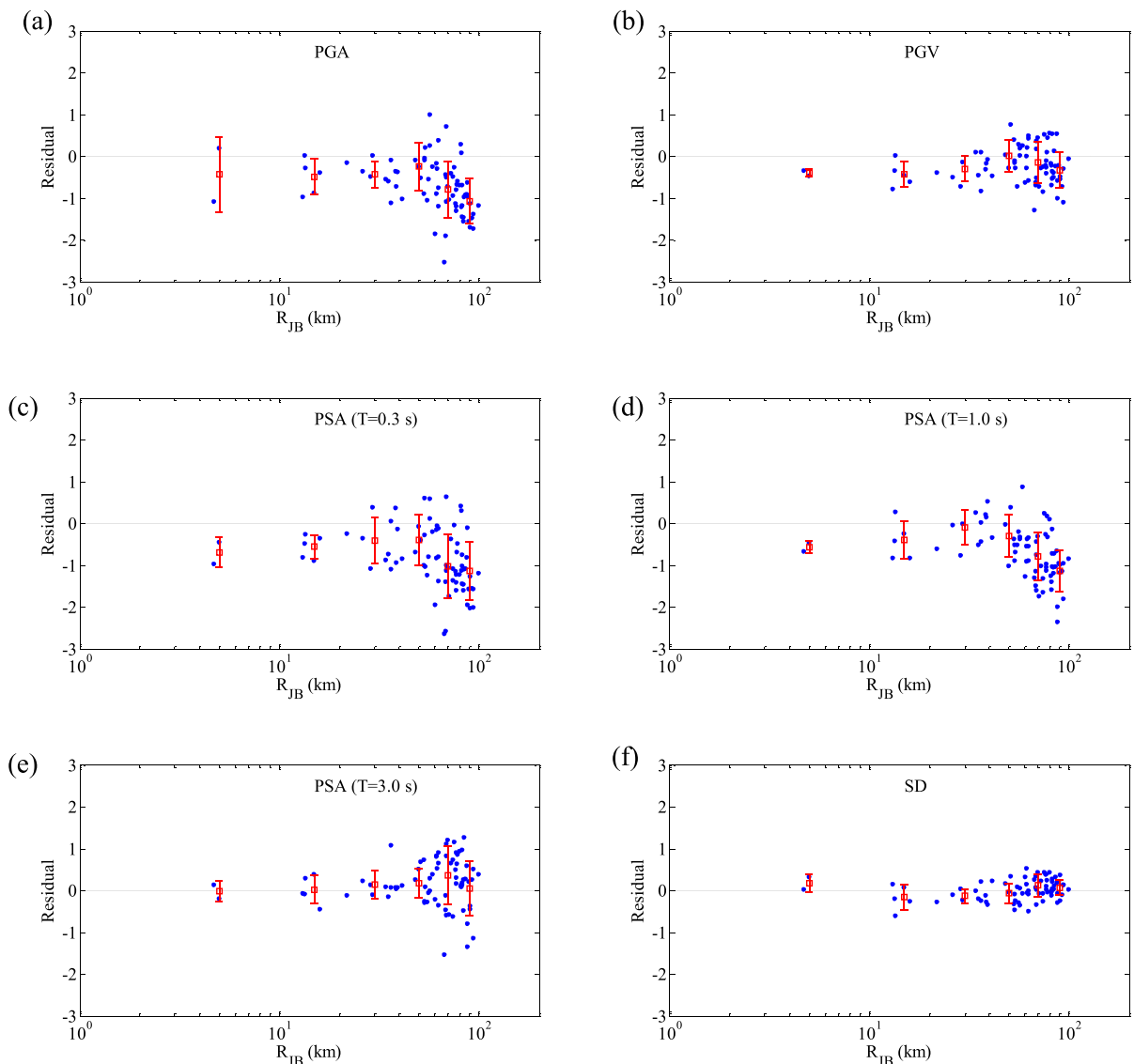


**Fig. 5** The residuals for (a) the observed PGAs, (b) PGVs, and (c–e) PSAs at periods of 0.3, 1.0, and 3.0 s, (f) SDs with predictions estimated by the BSSA14 and AS16 models. Red squares and red bars indicate the median and standard deviation binned by  $R_{JB}$

for distances larger than 60 km. This means that the distance trends go downward and the adjustment coefficients of anelastic attenuation are negative, indicating a relatively high-anelastic attenuation in the Menyuan region. For the PGVs, PSAs at long periods and SDs, the within-event residuals have flat distance trends. The within-event residuals for Central Italy 2016 earthquake sequence have similar characteristics with the Menyuan earthquake, and the characteristics are consistent with those in Luzi et al. (2017).

#### 4 Comparison of observed CSI with MMI and SMI

Ground motions are the fundamental cause of structural damage and casualties, and SMI is used to measure the degree of earthquake damage and ground motion shaking in an earthquake, as assessed by observed damages and human responses. With the availability of more and more ground motion records, the trend is becoming more

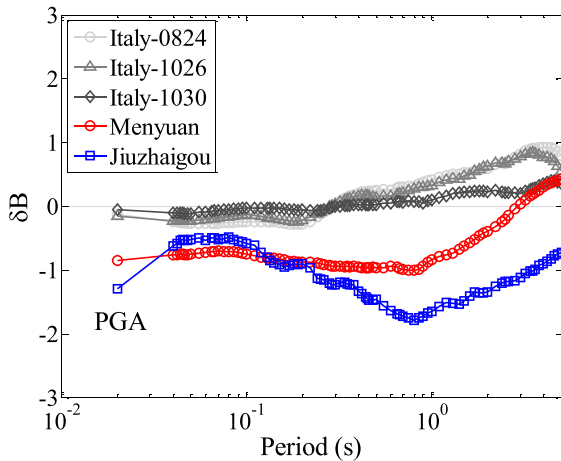


**Fig. 6** Between-event residuals for the PGAs and PSAs at periods up to 5.0 s for the Menyuan, Jiuzhaigou earthquake, and Central Italy 2016 earthquake sequence based on the BSSA14 model

and more obvious that instrumental seismic intensity based on GMICE is used to represent earthquake damage induced by ground motion. The most important application of GMICE is the various ShakeMap systems around the world (Wald et al. 1999; Worden et al. 2012; Caprio et al. 2015). Similar to MMI in ShakeMap, the CSI scale adopts PGA and PGV to calculate CSI from measured ground motion (GB/T 17742–2020 2020). The acceleration of each component is first band-passed filtered with a bandwidth of 0.1–10.0 Hz, then the maximal absolute acceleration and velocity of the vector composition of three components are used to calculate  $I_{PGA}$  and  $I_{PGV}$  as given in Eq. (1) where the units for acceleration and velocity are  $\text{cm/s}^2$  and  $\text{cm/s}$ , respectively.  $I_{PGV}$  is used to obtain CSI in the high-intensity area ( $\geq VI$ ), and the algebraic mean of  $I_{PGV}$  and  $I_{PGA}$  is used for CSI in the low-intensity area ( $< VI$ ), as given in Eq. (2).

$$\begin{aligned} I_{PGA} &= 3.17\log_{10}(a_{\max}) + 0.25 \\ I_{PGV} &= 3.00\log_{10}(v_{\max}) + 3.77 \end{aligned} \tag{1}$$

$$I = \begin{cases} I_{PGV} & \text{if } I_{PGA} \geq 6.0 \text{ and } I_{PGV} \geq 6.0 \\ (I_{PGA} + I_{PGV})/2 & \text{else} \end{cases} \tag{2}$$

The comparison of CSI and MMI calculated based on GMICE by Worden et al. (2012) is shown in Fig. 8a, and the CSI and MMI values are also listed in Table S1. Generally CSI values are higher than MMI values, and the gaps are even greater in high-intensity areas. The CSI at QHC0035 and QHC0036 stations are 1.4 intensity units greater than the MMI intensities. Though the PGAs at QHC0029 and QHC0036 stations are much smaller than QHC0028 station, the CSI at the two stations are basically the same as QHC0028 station, since the PGVs at these three stations are about the same size. But for MMI, the highest intensity is at QHC0028 station followed by QHC0029 then QHC0036 station. In this regard, PGV contributes more to CSI compared to MMI in the high-intensity area. Overall, CSI values are on average 0.73 intensity units greater than MMI values. Though CSI and MMI both have twelve seismic intensity scales from I to XII, the assessment of CSI and MMI are still different. For high seismic intensity  $\geq VI$ , intensity assessment is mainly based on building damage. Since the buildings types are different, and the seismic performance of buildings in California are better than those in China, the assessed CSI can be larger than MMI under the same level of ground motions. As shown in Table 1, for the same seismic intensity between VI and X+, the mean values of PGAs and PGVs for MMI are larger than those for CSI. In other words, the same PGAs and PGVs can calculate larger CSI than MMI. Immediate aftermath of the earthquake, structural engineers, and seismologists are dispatched to the affected area to assess the SMI. The isoseismic lines of SMI are shown in Fig. 1, and the SMI at ground motion stations are shown in Table S1. The scatter plot of SMI versus CSI based on instruments is shown in Fig. 8b. Since SMI values are reported as Roman numeral integers, in order to compare SMI and calculated CSI, the CSI values are rounded to the next Arabic integers. The RMS of the error between SMI and rounded CSI for SMI = V, VI, VII, and VIII are 1.0, 1.0, 0.7, and 0, respectively. The observed CSI predict very well SMI, especially for high SMI. It is noted that in the intensity VIII area, the rounded CSI from instruments are exactly the same as SMI.

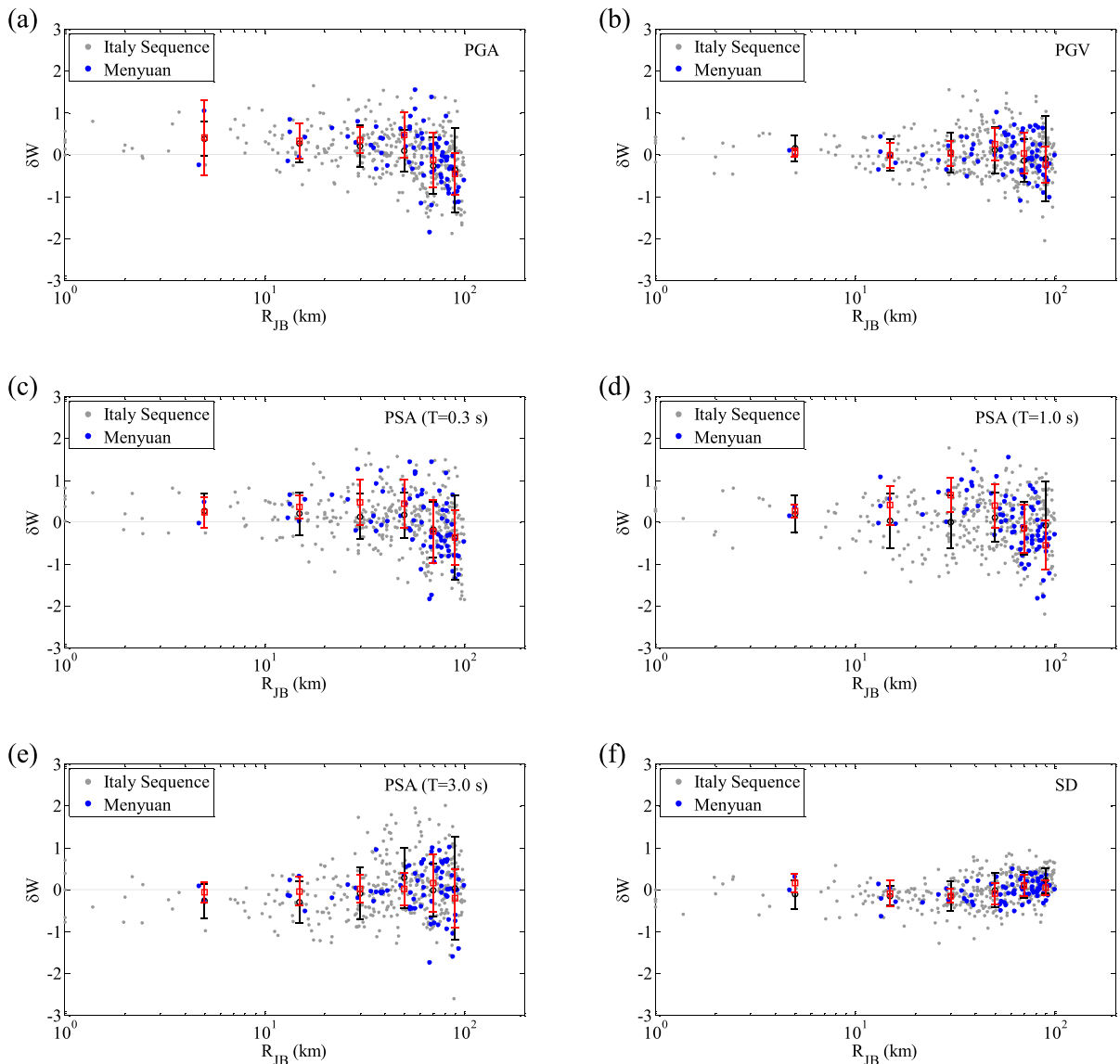


**Fig. 7** Within-event residuals for (a) the PGAs, (b) PGVs, and (c–e) PSAs at periods of 0.3, 1.0, and 3.0 s, (f) SD for the Menyuan earthquake and Central Italy 2016 earthquake sequence based on the BSSA14 and AS16 GMMs. Red squares and red bars indicate the median and standard deviation of

the Menyuan earthquake binned by  $R_{JB}$ , and black circles and black bars indicate the median and standard deviation of the Central Italy 2016 earthquake sequence binned by  $R_{JB}$ .  $R_{JB}$  equaling to 0 km is set to 1 km

## 5 Pulse classification

Near-field ground motions cause more potentially deformation and damage to structures than far-field with the same amplitude due to the distinct large velocity pulse (Bertero et al. 1978; Baltzopoulos et al. 2020). To find potentially impulsive characteristics of the near-field ground motions in the

Menyuan earthquake, the pulse classification methodology recently proposed by Baltzopoulos et al. (2020) is used to detect pulse-like ground motions. This methodology comprehensively considers both velocity waveform pulse extraction-based method and response spectral shape-based method, and it classifies a ground motion as pulse-like according to the following four criteria: (1) pulse indicator (PI)

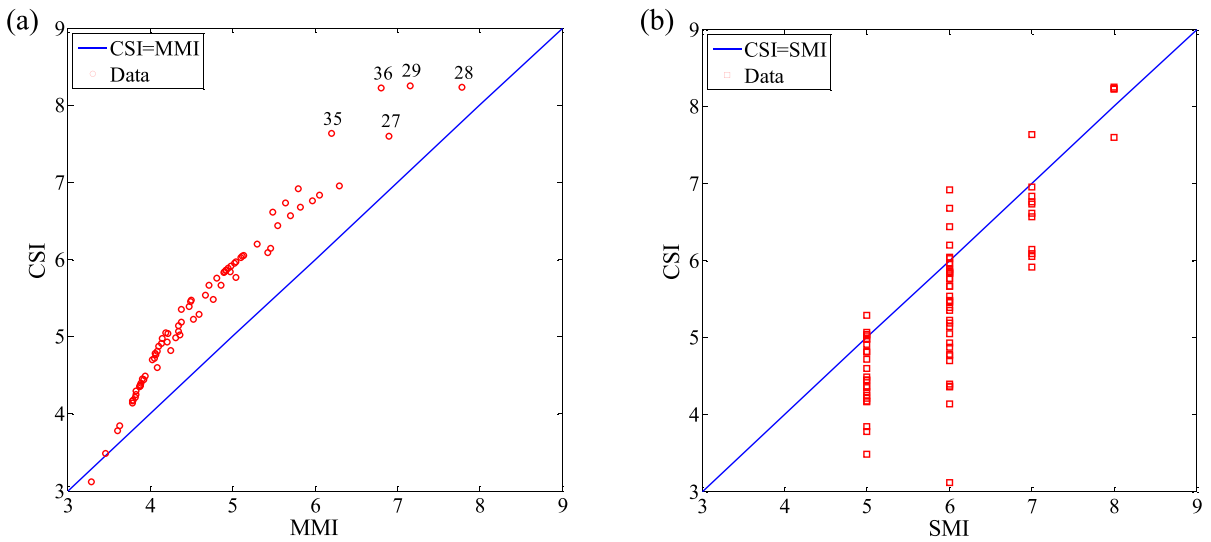


**Fig. 8** Comparison of Chinese seismic intensity (CSI) with surveyed macroseismic intensity (SMI) and MMI (a) CSI versus MMI; (b) CSI versus SMI. The numbers 27, 28, 29, 35, and 36 are for QHC0027, QHC0028, QHC0029, QHC0035, and QHC0036 stations

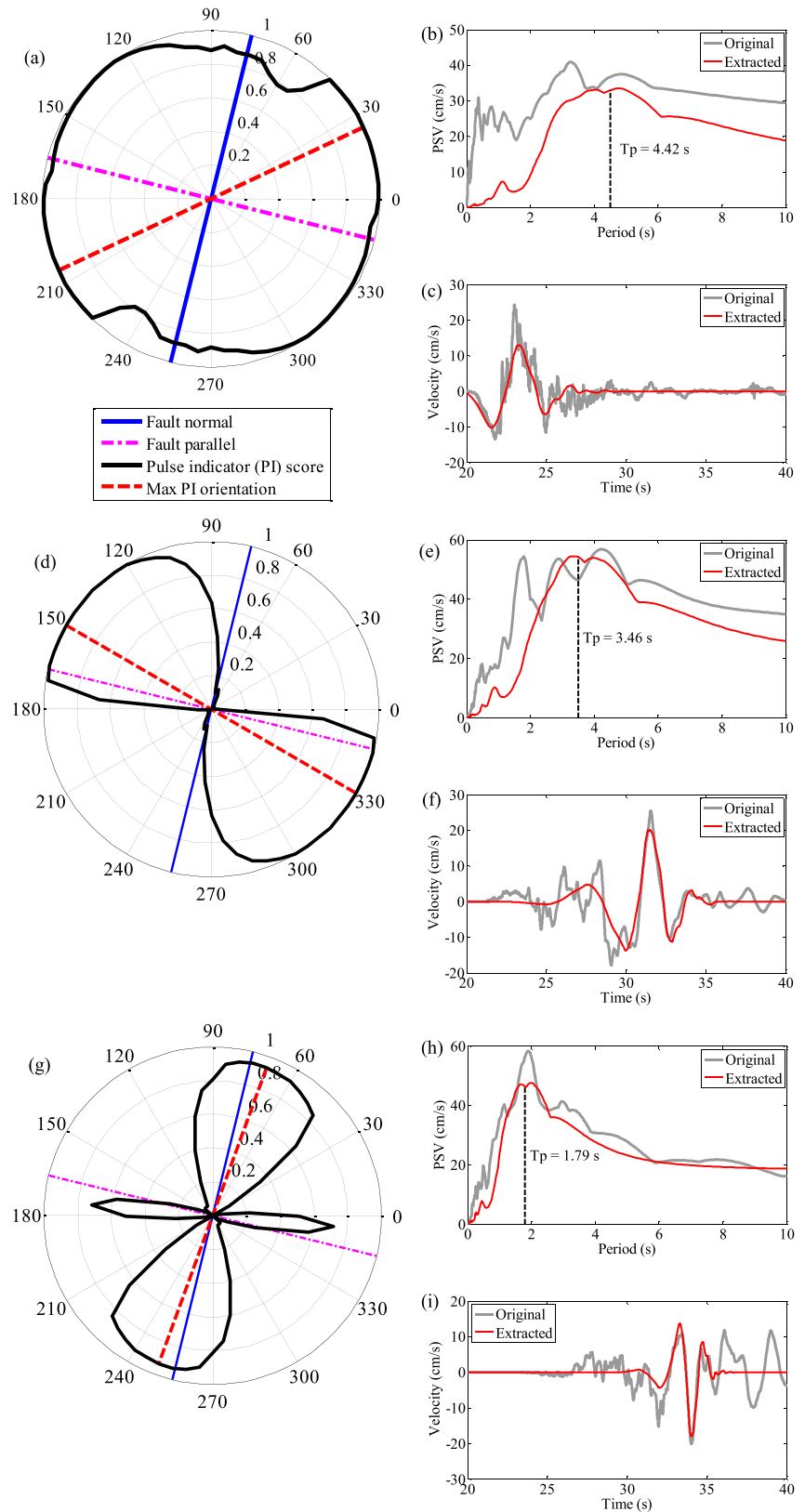
**Table 1** A comparison for ground motion parameters—seismic intensity in California and China

Intensity	I	II–III	IV	V	VI	VII	VIII	IX	X+
MMI PGA/(cm/s <sup>2</sup> )	<0.49	2.94	27	60.8	112.7	211	393	732	>1362
MMI PGV/(cm/s)	<0.02	0.13	1.41	4.65	9.64	20	41.4	85.8	>178
CSI PGA/(cm/s <sup>2</sup> )	<1.8	5.63	15.5	31.9	65.3	135	279	577	>1190
CSI PGV/(cm/s)	>0.12	0.41	1.2	2.59	5.57	12	25.8	55.5	>119

proposed by Baker (2007) is no less than 0.5; (2) high PI values persist over a consecutive range of orientations of two horizontal components; (3) the pseudo-spectral velocity (PSV) of the extracted pulse has good local fit to the PSV shape of the original ground motion at structural periods around pulse period  $T_p$ ; (4) the PGV of the extracted pulse is no less than 10 cm/s. Based on the above criteria, ground motions at stations QHC0028, QHC0036, and QHC0035 are classified as pulse-like. The PI polar plots of PI, PSVs, and velocities at the three stations are shown in Fig. 9. In the polar plot, the fault-parallel orientation shown with magenta color corresponds to the strike of 104° (here, 0° is for east direction, and 90° is for north direction). It is interesting that the PI scores at station QHC0028 are greater than 0.85 at almost all orientations except for a very small part between 50° and 65°, and this means that station QHC0028 has two impulsive characteristics along two perpendicular orientations. This behavior is also observed

at station China Lake mainshock record from 2019 Ridgecrest earthquake sequence (Baltzopoulos et al. 2020). Station QHC0036 only has  $PI \geq 0.85$  at orientations around fault-parallel direction, and station QHC0035 has smallest contiguous range of orientations around fault-parallel orientation with  $PI \geq 0.85$ . The corresponding extracted  $T_p$  at stations QHC0028, QHC0036, and QHC0035 are 4.42, 3.46, and 1.79 s, respectively. According to the  $T_p$  regression model by Chioccarelli and Iervolino (2013), the median  $T_p$  for  $M_w$  6.6 is 2.39 s with a plus/minus natural logarithm standard deviation interval of 1.33–4.3 s.  $T_p$  at stations QHC0028 is a slightly larger than median plus one standard deviation, whereas the other two  $T_p$  fall well between one standard deviation interval. The spatial distribution of pulse-like and nonpulse-like records, relative to the finite-fault geometry of the Menyuan earthquake, is shown in Fig. 10a. QHC0036 and QHC0035 stations are located along the extension of the fault toward the northern end of the rupture,

**Fig. 9** Polar plot of (a) pulse indicator (PI), (b) pseudo-spectral velocity (PSV), and (c) velocity time histories at the orientation with maximum PI at station QHC0028 (d–f) and (g–i) corresponding plots at station QHC0036 and QHC0035, respectively





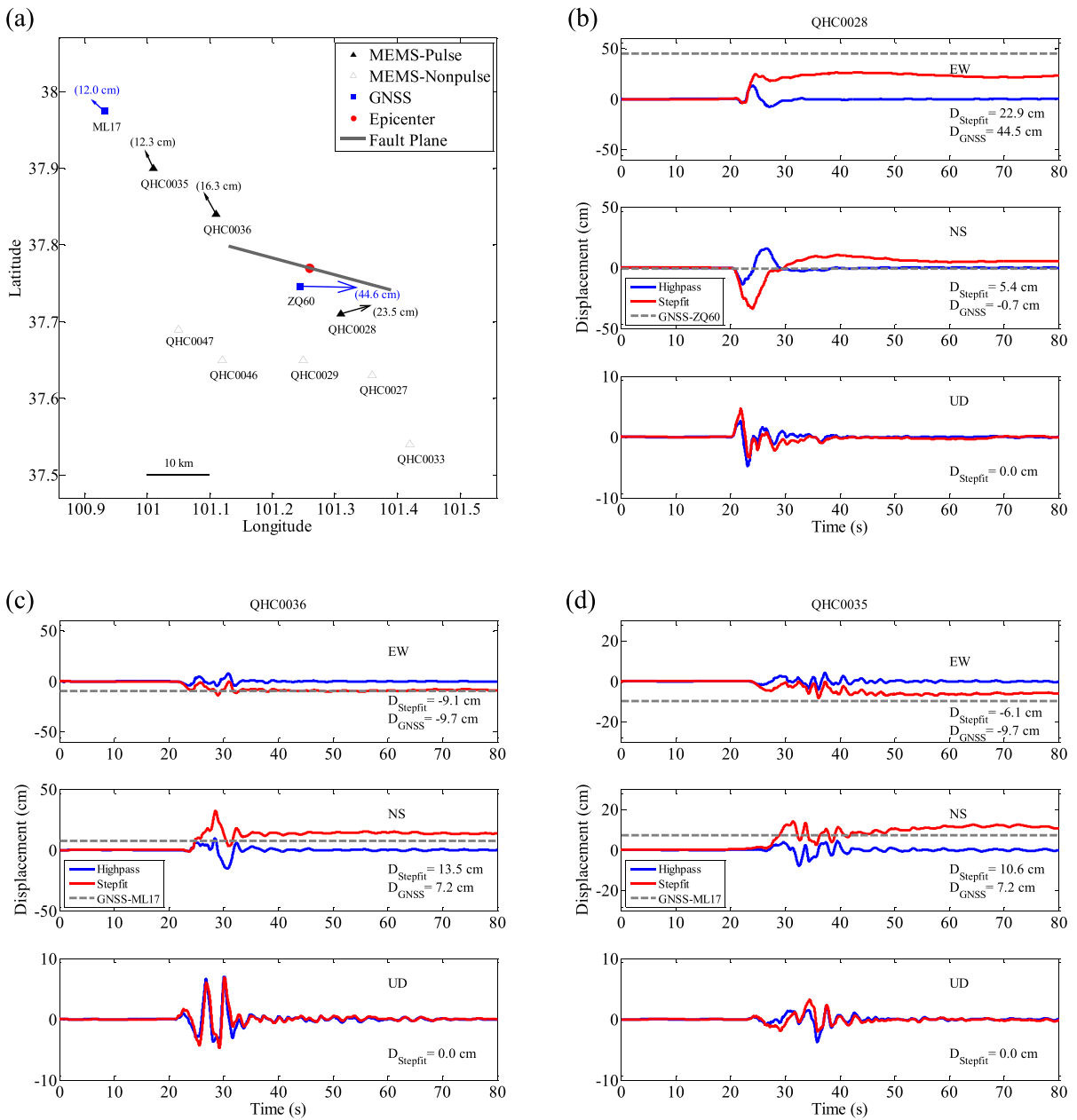


**Fig. 10** Spatial distribution of pulse-like ground motions and comparison of processed displacements with permanent static offsets from GNSS. **a** MEMS stations classified as pulse-like and nonpulse-like together with two GNSS stations giving permanent horizontal displacements, with arrows showing the directions and the numbers in parentheses showing displacements

and QHC0028 station is along the fault toward south and is close to the epicenter. If fault-normal pulse is defined as the record of which highest PI falls within  $30^\circ$  of the strike normal, and fault-parallel pulse is

defined when highest PI falls within  $30^\circ$  of the strike parallel according to the definition by Baltzopoulos et al. (2020), ground motions at station QHC0035 are regarded as fault-normal pulse, and those at station

QHC0036 as fault-parallel pulse. However, ground motions at station QHC0028 are neither fault-normal nor fault-parallel pulse. It is noted that for strike-slip ruptures, pulse-like ground motions can be observed in orientations other than fault-normal direction (e.g., Baltzopoulos et al. 2020).

Since fling step may also cause impulsive characteristics in near-field ground motions, it is necessary to check the permanent static displacements near the fault. The StepFit method proposed by Wang et al. (2011) and implemented in a function `baselineK.m` by Melgar et al. (2013) are used to correct strong motion accelerogram for baseline offset. The StepFit method fits a step function to find the best value of the start and end time of significant acceleration pulse, and has been tested to successfully correct record of a low-cost MEMS sensor (Wang et al. (2011)). To keep the low-frequency content included in permanent displacements, the near-field acceleration records are only removed the pre-event noise mean and not processed with any band-passed filtering before ingested into the `baselineK.m` function. The directions and values of processed permanent displacements at QHC0028, QHC0036, and QHC0035 stations are shown in Fig. 10a, and the corresponding displacement time histories, compared with permanent horizontal offsets observed at the global navigation satellite system (GNSS) stations, are shown in Fig. 10b–d. The displacements processed by high-pass filtering with cutting frequency of 0.1 Hz are also shown as references. QHC0028 station is 7.0 km away from GNSS station ZQ60, and QHC0036 and QHC0035 stations are 21.6 km and 10.7 km away from GNSS station ML17, respectively. The processed permanent displacements at QHC0036 and QHC0035 stations are close to the static offsets of GNSS station ML17, while the processed permanent displacements at station QHC0028 are much smaller than the static offsets of GNSS station ZQ60. However, in general, the directions of permanent displacements at these three MEMS stations are consistent with the corresponding nearby GNSS stations. The maximum EW component permanent displacement is obtained at station QHC0028 (22.9 cm on the east [E] component), and the maximum NS component permanent displacement is obtained at station QHC0036 (13.5 cm on the north [N] component). The UD component permanent displacements are negligible.

It can be seen that the permanent displacement is along a direction similar to the max PI orientation of the pulse for station QHC0028 and QHC0036, respectively, as shown in Fig. 9a and d. While for station QHC0035, the permanent displacements is along a direction similar to the perpendicular of the max PI orientation of the pulse as shown in Fig. 9g, and the cause of pulse can be related to forward directivity effect. The impulse characteristics at stations QHC0028 and QHC0036 may have been influenced by fling step. But from Fig. 9c and f, the velocities show clearly double-sided pulses, which is incompatible with one-sided pulse by fling step. The cause of these pulses, forward directivity or fling step, needs to be further investigated. Baltzopoulos et al. (2020) found similar results for two stations (CCC and MPM) in 2019 Ridgecrest earthquake sequence, and also stated that the origin for the pulses required further investigation.

## 6 Earthquake Damage of a high-speed railway bridge

The area of Menyuan County is classified as VIII seismic intensity (0.2 g) for design basis earthquake, and the design characteristic period of

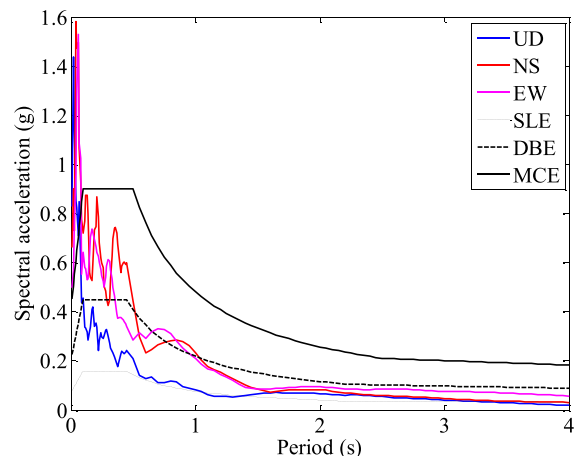


**Fig. 11** Acceleration response spectra with 5% damping ratio at QHC0028 station. The blue line is UD component, the red line is NS component, the magenta line is EW component, the gray dash-dot line is SLE (service level earthquake), the gray dashed line is DBE (design basis earthquake), and the gray solid line is MCE (maximum credible earthquake)

ground motion is 0.40 s for site category II in China (see Data and resources). The acceleration response spectra at the short period range below 0.5 s are quite significant shown in Fig. 11, implying that the ground motions can cause heavy damage to low-rise masonry buildings. However, for period larger than 1.0 s, the acceleration response spectra do not exceed the line of design basis earthquake, implying that the ground motions may not cause damage to mid-rise and high-rise reinforced concrete and steel buildings. As the event occurred in a sparsely populated area, there were few reported damaged buildings in the epicenter area. There was a high-speed railway bridge called Liuhuanggou bridge about 10 km away from QHC0028 station, and it was 7 km away from the epicenter, as shown in Fig. 1. The bridge was an 8-span 32 m simply supported girder bridge, and it was severely damaged due to the failure of bearings shown in Fig. 12. It is unclear whether the failure of bearings is due to large

velocity pulse or reciprocating action of ground motion. Since the ground motion at QHC0028 station were pulse-like at almost all orientations, it is possible that the bearings lost bearing capacity as shear deformation exceed the limit cause by the distinct large velocity pulse. It has been reported that the bearings were damaged by near-field ground motions (e.g., the bearings of Hamate Bypass were seriously damaged in 1995 Kobe earthquake (Chung et al. 1996); the sliding pot bearings of Bolu viaduct were damaged in 1999 Duzce earthquake (Park et al. 2004). With the failure of bearings, the girders slipped from the bearings as a rigid body, causing the bridge decks on both sides of the pier to dislocate and resulting in track to be twisted and fractured. However, the girders and piers were basically intact in the earthquake. Since the design of simply supported girder bridges for high-speed railways in China takes the ride comfort as the primary goal, the girders and piers are designed much stiffer

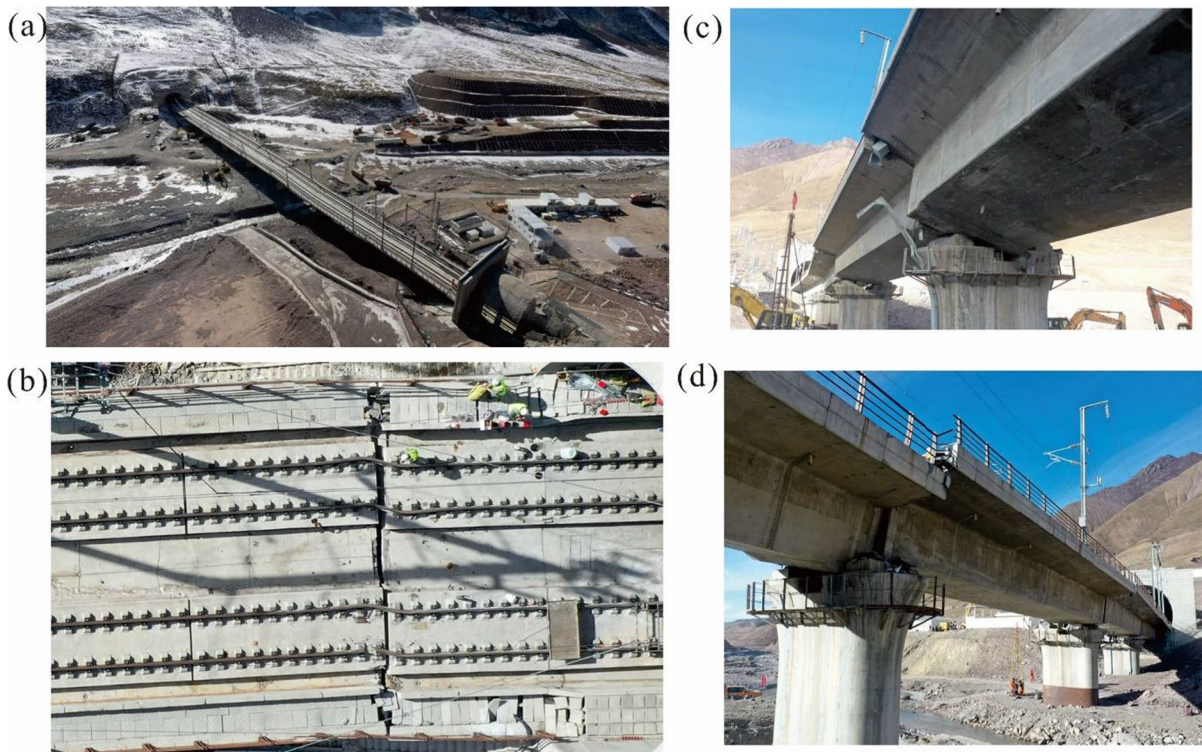


**Fig. 12** Earthquake damage photos for Liuhuanggou high-speed railway bridge. **a** Aerial view; **b** twisted and fractured tracks; **c** lateral shift and deflection of the girders; **d** destroyed failure (see Data and resources)

and stronger than ordinary railway bridges (Guo et al. 2020). In this regard, the bearings could be the weakest part, and more attention should be paid to the seismic design of the high-speed railway bridge bearings. The severe damage of the high-speed railway bridge resulted in suspension of Lanzhou-Xinjiang high-speed trains. For further research, the ground motions at the bridge site should be simulated to check if the ground motions are impulsive or not, and finite element model of the bridge and nonlinear time history analysis should be built and conducted to investigate the failure process of the bearings.

## 7 Conclusions

The 8 January 2022  $M_S$  6.9 Menyuan earthquake was recorded by a large number of MEMS stations within 100-km Joyner-Boore fault distance. The strong motion records provided a database for analyzing the main features of the ground motions measured by MEMS stations, in terms of time–frequency energy distributions, GMMs, near-field impulsive characteristics, and seismic intensities.

By comparing the pre-event noises and earthquake signals in time domain and frequency domain, it is found that the ground motion records have good SNR and the frequency contents in 0.1–20 Hz are credible, and the records are feasible to be used to analyze ground motion parameters. Time–frequency energy distributions of the nearest stations with  $R_{JB} \sim 10$  km show quite different characteristics of high-frequency contents, implying strong attenuation for high frequency in the close near-field.

The ground motion parameters such as horizontal vector PGAs, PGVs, PSAs, and SDs are compared with the predicted values by the BSSA14 and AS16 GMMs. The PGAs and PSAs at short and medium periods of 0.3 s and 1.0 s are noticeably overestimated by the BSSA14 model, and PSAs at long-period 3.0 s are consistent with the prediction model. The PGVs and SDs are well predicted by the two GMM models. According to the analysis of between-event residuals, the BSSA14 model predicts higher shaking at the short and medium periods and lower shaking in the long periods for the Menyuan earthquake, while predicts higher shaking in the whole analyzed periods for the Jiuzhaigou earthquake. On the other hand,

the PGAs and PSAs at periods of no more than 1.0 s are well predicted by the BSSA14 model for Central Italy 2016 earthquake sequence. The characteristics of within-event residuals are similar for the Menyuan earthquake and Italy sequence. For the PGAs and PSAs at short periods, the within-event residuals have positive trends at short distances while negative trends for distances larger than 60 km. For the PGVs, PSAs at long periods and SDs, the within-event residuals have flat distance trends.

According to comparison of observed CSI from instruments with MMI and on-site SMI, CSI values are 0.73 intensity units greater than MMI values on average, and CSI predict very well SMI, especially in high seismic intensity region. Ground motion records at three stations are classified as pulse-like based on the methodology by Baltzopoulos et al. (2020). Ground motions at QHC0035 station are identified as fault-normal pulse, and those at QHC0036 station as fault-parallel pulse. Ground motion at QHC0028 station have pulse indicator greater than 0.85 at almost all orientations. By discussing the forward directivity and fling step on the pulses, only one station may be directivity effect-related and the other two are still inconclusive. Finally, the earthquake damage of a high-speed railway bridge, which includes bearings failure, twisted, and fractured tracks, is presented. The ground motion at bridge site should be simulated to check if the bearings are damaged by large velocity pulse or reciprocating action of the ground motion for further study. The MEMS-based station is a proper supplement to the traditional FBA-based station, and in the future, more near-field data will be obtained from MEMS-based stations, providing a larger database for analyzing the characteristics of near-field ground motions and damage potentials thereof.

**Acknowledgements** The comments of two anonymous reviewers and associated editor are very helpful for improving the quality of the article.

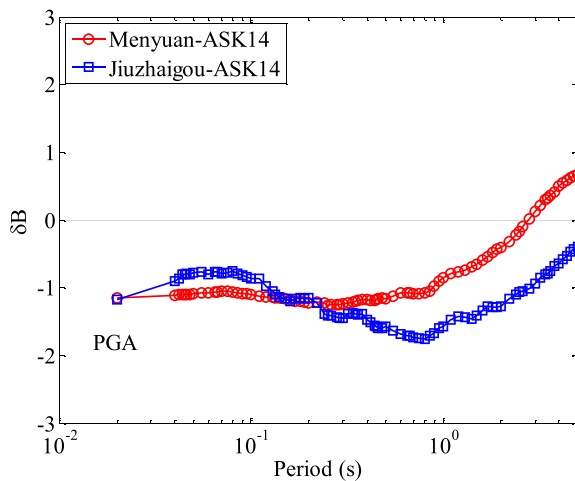
**Funding** This research was partially supported by Scientific Research Fund of Institute of Engineering Mechanics, China Earthquake Administration (grant No. 2021B08), and National Natural Science Foundation of China (grant No. U2039209 and 5150082083).

**Declarations**

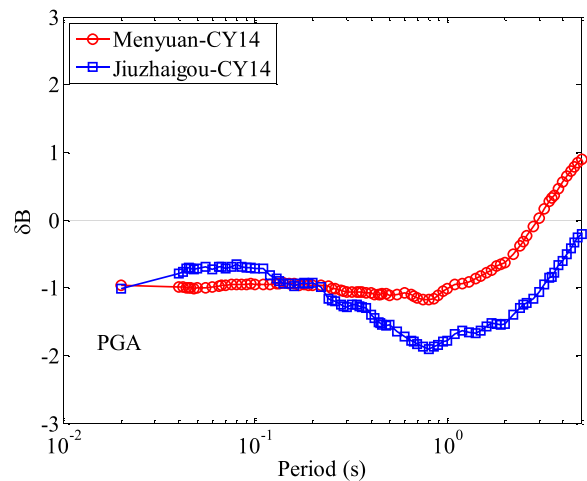
**Competing interests** The authors declare no competing interests.



## Appendix



(a) ASK14 model



(b) CY14 model

**Fig. 13** Between-event residuals for the PGAs and PSAs at periods up to 5.0 s for the Menyuan and Jiuzhaigou earthquakes based on the Abrahamson et al. (2014) (hereinafter

ASK14) and Chiou and Youngs (2014) (hereinafter CY14) models. **(a)** ASK14 model, **(b)** CY14 model

## References

- Abrahamson NA, Silva WJ, Kamai R (2014) Summary of the ASK14 ground motion relation for active crustal regions. *Earthq Spectra* 30(3):1025–1055. <https://doi.org/10.1193/070913EQS198M>
- Afshari K, Stewart JP (2016) Physically parameterized prediction equations for significant duration in active crustal regions. *Earthq Spectra* 32(4):2057–2081. <https://doi.org/10.1193/063015EQS106M>
- Al Atik L, Abrahamson N, Bommer JJ, Scherbaum F, Cotton F, Kuehn N (2010) The variability of ground-motion prediction models and its components. *Seismol Res Lett* 81:794–801. <https://doi.org/10.1785/gssrl.81.5.794>
- Baker JW (2007) Quantitative classification of near-fault ground motions using wavelet analysis. *Bull Seismol Soc Am* 97(5):1486–1501. <https://doi.org/10.1785/0120060255>
- Baltzopoulos G, Luzzi L, Iervolino I (2020) Analysis of near-source ground motion from the 2019 Ridgecrest earthquake sequence. *Bull Seismol Soc Am* 110(4):1495–1505. <https://doi.org/10.1785/0120200038>
- Bertero VV, Mahin SA, Herrera RA (1978) Aseismic design implications of near-fault San Fernando earthquake records. *Earthq Eng Struct Dynam* 6(1):31–42. <https://doi.org/10.1002/eqe.4290060105>
- Boore DM (2010) Orientation-independent, nongeometric-mean measures of seismic intensity from two horizontal components of motion. *Bull Seismol Soc Am* 100(4):1830–1835. <https://doi.org/10.1785/0120090400>
- Boore DM, Stewart JP, Seyhan E, Atkinson GM (2014) NGA-west2 equations for predicting PGA, PGV, and 5% damped PSA for shallow crustal earthquakes. *Earthq Spectra* 30(3):1057–1085. <https://doi.org/10.1193/070113EQS184M>
- Buckheit JB, Donoho DL (1995) WaveLab and reproducible research. In: Antoniadis A, Oppenheim G (eds) *Wavelets in statistics*. Springer-Verlag, New York, pp 55–82
- Caprio M, Tarigan B, Worden CB, Wiemer S, Wald DJ (2015) Ground motion to intensity conversion equations (GMICEs): a global relationship and evaluation of regional dependency. *Bull Seismol Soc Am* 105(2):1–21. <https://doi.org/10.1785/0120140286>
- Chioccarelli E, Iervolino I (2013) Near-source seismic hazard and design scenarios. *Earthq Eng Struct Dynam* 42(4):603–622. <https://doi.org/10.1002/eqe.2232>
- Chiou BS-J, Youngs RR (2014) Update of the Chiou and Youngs NGA model for the average horizontal component of peak ground motion and response spectra. *Earthq Spectra* 30(3):1117–1153. <https://doi.org/10.1193/072813EQS219M>
- Chung R, Ballantyne D, Comeau E, Holzer T, Madrzykowski D, Schiff A, Stone W, Wilcoski J, Borchardt R, Cooper J, Lew H, Moehle J, Sheng L, Taylor A, Bucker I, Hayes JJ, Leyendecker E, O'Rourke T, Singh M, Whitney M (1996) January 17, 1995 Hyogoken-Nanbu (Kobe) Earthquake: performance of structures, lifelines, and fire protection systems (NIST SP 901), special publication (NIST SP), National Institute of Standards and Technology, Gaithersburg, MD. <https://doi.org/10.6028/NIST.SP.901>, <https://doi.org/10.6028/NIST.SP.901>

- [tsapps.nist.gov/publication/get\\_pdf.cfm?pub\\_id=910273](https://tsapps.nist.gov/publication/get_pdf.cfm?pub_id=910273). Accessed June 13, 2022
- Clayton RW, Heaton T, Kohler M, Chandy M, Guy R, Bunn J (2015) Community seismic network: a dense array to sense earthquake strong motion. *Seismol Res Lett* 86(5):1354–1363. <https://doi.org/10.1785/0220150094>
- Cochran E, Lawrence J, Christensen C, Chung A (2009) A novel strong-motion seismic network for community participation in earthquake monitoring. *IEEE Instru Meas Mag* 12(6):8–15. <https://doi.org/10.1109/MIM.2009.5338255>
- Cochran E, Lawrence J, Kaiser A, Fry B, Chung A, Christensen C (2011) Comparison between low-cost and traditional MEMS accelerometers: a case study from the M7.1 Darfield, New Zealand, aftershock deployment. *Ann Geophys* 54(6). <https://doi.org/10.4401/ag-5268>
- Deng Q, Zhang P, Ran Y, Yang X, Min W, Chu Q (2003) Basic characteristics of active tectonics of China. *Sci China Earth Sci* 46(4):356–373
- Engler DT, Worden CB, Thompson EM, Jaiswal KS (2022) Partitioning ground motion uncertainty when conditioned on station data. *Bull Seismol Soc Am* XX:1–20. <https://doi.org/10.1785/0120210177>
- Evans JR, Allen RM, Chung AI, Cochran ES, Guy G, Hellweg M, Lawrence JF (2014) Performance of several low-cost accelerometers. *Seismol Res Lett* 85(1):147–158. <https://doi.org/10.1785/0220130091>
- Filippitzi F, Kohler M, Heaton T, Graves R, Clayton R, Guy R, Bunn J, Chandy M (2021) Ground motions in urban Los Angeles from the 2019 Ridgecrest earthquake sequence. *Earthq Spectra* 37(4):2493–2522. <https://doi.org/10.1177/87552930211003916>
- Fleming K, Picozzi M, Milkereit C, Kühnlenz F, Lichtblau B, Fischer J, Zulfikar C, Özel O, the SAFER and EDIM working groups (2009) The self-organizing seismic early warning information network (SOSEWIN). *Seismol Res Lett* 80(5):755–771. <https://doi.org/10.1785/gssrl.80.5.755>
- GB/T 17742–2020 (2020) The Chinese seismic intensity scale. Standard Press of China, Beijing (in Chinese)
- Guo W, Du QD, Huang Z, Gou HY, Xie X, Li Y (2020) An improved equivalent energy-based design procedure for seismic isolation system of simply supported bridge in China's high-speed railway. *Soil Dyn Earthq Eng* 134:10616. <https://doi.org/10.1016/j.soildyn.2020.106161>
- Holland A (2003) Earthquake data recorded by the MEMS accelerometer: field testing in Idaho. *Seismol Res Lett* 74(1):20–26. <https://doi.org/10.1785/gssrl.74.1.20>
- Hough SE, Thompson E, Parker GA, Graves RW, Hudnut KW, Patton J, Dawson T, Ladinsky T, Oskin M, Sirorattanakul K et al (2020a) Near-field ground motions from the July 2019 Ridgecrest, California, earthquake sequence. *Seismol Res Lett* 91(3):1542–1555. <https://doi.org/10.1785/0220190279>
- Hough SE, Yun SH, Jung J, Thompson E, Parker GA, Stephenson O (2020b) Near-field ground motions and shaking from the 2019 Mw 7.1 Ridgecrest, California, mainshock: insights from instrumental, macroseismic intensity, and remote-sensing data. *Bull Seismol Soc Am* 110(4):1506–1516. <https://doi.org/10.1785/0120200045>
- Kohler MD, Philippitzi F, Heaton T, Clayton RW, Guy R, Bunn J, Chandy KM (2020) 2019 Ridgecrest earthquake reveals areas of Los Angeles that amplify shaking of high-rises. *Seismol Res Lett* 91(6):3370–3380. <https://doi.org/10.1785/0220200170>
- Li H, Tao D, Huang Y, Bao Y (2013) A data-driven approach for seismic damage detection of shear-type building structures using the fractal dimension of time–frequency features. *Struct Control Health Monit* 20(9):1191–1210. <https://doi.org/10.1002/stc.1528>
- Luzi L, Pacor F, Puglia R, Lanzano G, Felicetta C, D'Amico M, Michelini A, Faenza L, Lauciani V, Iervolino I, Baltzopoulos G, Chioccarelli E (2017) The central Italy seismic sequence between August and December 2016: analysis of strong-motion observations. *Seismol Res Lett* 88(5):1219–1231. <https://doi.org/10.1785/0220170037>
- Melgar D, Bock Y, Sanchez D, Crowell BW (2013) On robust and automated baseline corrections for strong motion seismology. *J Geophys Res* 118(3):1177–1187. <https://doi.org/10.1002/jgrb.50135>
- Nof RN, Chung AI, Rademacher H, Dengler L, Allen RM (2019) MEMS accelerometer mini-array (MAMA): a low-cost implementation for earthquake early warning enhancement. *Earthq Spectra* 35(1):21–38. <https://doi.org/10.1785/0220190097>
- Park SW, Ghasemi H, Shen J, Somerville PG, Yen WP, Yashinsky M (2004) Simulation of the seismic performance of the Bolu Viaduct subjected to near-fault ground motions. *Earthquake Eng Struct Dynam* 33(13):1249–1270. <https://doi.org/10.1002/eqe.395>
- Peng C, Jiang P, Chen Q, Ma Q, Yang J (2019) Performance evaluation of a dense MEMS-based seismic sensor array deployed in the Sichuan-Yunnan border region for earthquake early warning. *Micromachines* 10(11):735. <https://doi.org/10.3390/mi10110735>
- Peng C, Ma Q, Jiang P, Huang W, Yang D, Peng H, Chen L, Yang J (2020) Performance of a hybrid demonstration earthquake early warning system in the Sichuan-Yunnan border region. *Seismol Res Lett* 91(2A):835–846. <https://doi.org/10.1785/0220190101>
- Pierleoni P, Marzorati S, Ladina C, Raggiunto S, Belli A, Palma L, Cattaneo M, Valenti S (2018) Performance evaluation of a low-cost sensing unit for seismic applications: field testing during seismic events of 2016–2017 in Central Italy. *IEEE Sens J* 18(16):6644–6659. <https://doi.org/10.1109/JSEN.2018.2850065>
- Ren Y, Wang H, Xu P, Dhakal YP, Wen R, Ma Q, Jiang P (2018) Strong-motion observations of the 2017 Ms 7.0 Jiuzhaigou earthquake: comparison with the 2013 Ms 7.0 Lushan earthquake. *Seismol Res Lett* 89(4):1354–1365. <https://doi.org/10.1785/0220170238>
- Trifunac MD, Brady AG (1975) A study on the duration of strong ground motion. *Bull Seismol Soc Am* 65:581–626
- Wald DJ, Allen TI (2007) Topographic slope as a proxy for seismic site conditions and amplification. *Bull Seismol Soc Am* 97(5):1379–1395. <https://doi.org/10.1785/0120060267>
- Wald DJ, Quitoriano V, Dengler L, Dewey JW (1999) Utilization of the internet for rapid community intensity maps. *Seismol Res Lett* 70(6):680–697. <https://doi.org/10.1785/gssrl.70.6.680>
- Wang RJ, Schurr B, Milkereit C, Shao ZG, Jin MP (2011) An improved automatic scheme for empirical baseline



- correction of digital strong-motion records. *Bull Seismol Soc Am* 101(5):2029–2044. <https://doi.org/10.1785/0120110039>
- Wen R, Ren Y (2014) Strong-motion observations of the Lushan earthquake on 20 April 2013. *Seismol Res Lett* 85(5):1043–1055. <https://doi.org/10.1785/0220140006>
- Wen ZP, Xie JJ, Gao MT, Hu YX, Chau KT (2010) Near-source strong ground motion characteristics of the 2008 Wenchuan earthquake. *Bull Seismol Soc Am* 100(5B):2425–2439. <https://doi.org/10.1785/0120090266>
- Wessel P, Luis JF, Uieda L, Scharroo R, Wobbe F, Smith WHF, Tian D (2019) The generic mapping tools version 6. *Geochem Geophys Geosy* 20(11):5556–5564. <https://doi.org/10.1029/2019GC008515>
- Worden CB, Gerstenberger MC, Rhoades DA, Wald DJ (2012) Probabilistic relationships between ground-motion parameters and modified Mercalli intensity in California. *Bull Seismol Soc Am* 102:204–221. <https://doi.org/10.1785/0120110156>
- Wu YM, Chen DY, Lin TL, Hsieh CY, Chin TL, Chang WY, Li WS, Ker SH (2013) A high-density seismic network for earthquake early warning in Taiwan based on low cost sensor. *Seismol Res Lett* 84(6):1048–1054
- Wu YM, Liang WT, Mittal H, Chao WA, Lin CH, Huang BS, Lin CM (2016) Performance of a low-cost earthquake early warning system (P-Alert) during the 2016  $M_L$  6.4 Meinong (Taiwan) earthquake. *Seismol Res Lett* 87(5):1050–1059. <https://doi.org/10.1785/0220160058>
- Yildirim B, Cochran E, Chung A, Christensen C, Lawrence J (2015) On the reliability of Quake-Catcher Network earthquake detections. *Seismol Res Lett* 86(3):856–869. <https://doi.org/10.1785/0220140218>
- Zhang Y, Shan X, Zhang G, Zhong M, Zhao Y, Wen S, Qu C, Zhao D (2020) The 2016  $M_w$  5.9 Menyuan earthquake in the Qilian Orogen, China: a potentially delayed depth-segmented rupture following from the 1986  $M_w$  6.0 Menyuan Earthquake. *Seismol Res Lett* 91(2A):758–769. <https://doi.org/10.1785/0220190168>
- Zhang Y, Xu LS, Chen YT (2022) Earthquake of magnitude 6.9 in Menyuan, Qianghai 8 January 2022, available at <https://www.cea-igp.ac.cn/kydt/278809.html>. last accessed February 2022, in Chinese
- Zhou Z, Adeli H (2003) Time-frequency signal analysis of earthquake records using Mexican hat wavelets. *Comput-Aided Civ Inf* 18:379–389. <https://doi.org/10.1111/1467-8667.t01-1-00315>
- Publisher's note** Springer Nature remains neutral with regard to jurisdictional claims in published maps and institutional affiliations.
- Data and resources** MEMS strong motion data for this study were provided by China Strong Motion Network Center at the Institute of Engineering Mechanics, China Earthquake Administration. The SMI map is available at <https://www.cea.gov.cn/cea/xwzx/fzjzyw/5646200/index.html> (in Chinese). Surface ruptures from the remote sensing image by National Institute of Natural Hazards is available at [http://www.ninhm.ac.cn/content/details\\_35\\_3079.html](http://www.ninhm.ac.cn/content/details_35_3079.html) (in Chinese). The Earthquake damage photos for Liuhuanggou high-speed railway bridge provided by Institute of Engineering Mechanics, China Earthquake Administration, are available at <https://www.iem.ac.cn/detail.html?id=2340> (in Chinese). The finite fault model is available at <https://www.cea-igp.ac.cn/kydt/278809.html> (in Chinese). The seismic intensity and design characteristic period for design basis earthquake are available at <http://www.gb18306.net/> (in Chinese). The global  $V_{S30}$  data provided by USGS is available at <https://earthquake.usgs.gov/data/vs30/>. The programs to calculate predicted ground motion parameters by the BSSA14, ASK14, CY14, and AS16 GMMs are available at [https://www.daveboore.com/software\\_online.html](https://www.daveboore.com/software_online.html) and <https://github.com/bakerjw/GMMs>. Pulse identification algorithm in Baker (2007) is available at [https://www.jackwbaker.com/pulse-classification\\_old.html](https://www.jackwbaker.com/pulse-classification_old.html). The StepFit method to correct strong motion accelerogram for baseline offset is available at <https://github.com/dmelgarm/baselineK>. The flatfile with the strong-motion parameters for Central Italy 2016 earthquake sequence is available at <http://esm.mi.ingv.it/flatfile-2017/>. All of the above websites were last accessed February 2022. WaveLab package to produce time–frequency energy distributions was obtained from [https://statweb.stanford.edu/~wavelab/Wavelab\\_850/pdownload.html](https://statweb.stanford.edu/~wavelab/Wavelab_850/pdownload.html) (last accessed March 2018; however, the access permission for package download is denied in June 2022). Some of the plots were produced using Generic Mapping Tools (version 6) (Wessel et al. 2019).

Springer Nature or its licensor holds exclusive rights to this article under a publishing agreement with the author(s) or other rightsholder(s); author self-archiving of the accepted manuscript version of this article is solely governed by the terms of such publishing agreement and applicable law.